A simple and effective method for fabricating novel p–n heterojunction photocatalyst g-C$_3$N$_4$/Bi$_4$Ti$_3$O$_{12}$ and its photocatalytic performances

Yang Guo [a], Jinhai Li [a], Zhanqi Gao [a,b], Xin Zhu [a,c], Ying Liu [a], Zhongbo Wei [a], Wei Zhao [a], Cheng Sun [a,*]

[a] State Key Laboratory of Pollution Control and Resource Reuse, School of the Environment Nanjing University, Nanjing 210023, PR China
[b] Environmental Monitoring Center of Jiangsu Province, Nanjing 210036, PR China
[c] Nanjing Institute of Environmental Science, Ministry of Environmental Protection of China, Nanjing 210042, PR China

ARTICLE INFO

ABSTRACT

A novel g-C$_3$N$_4$/Bi$_4$Ti$_3$O$_{12}$ photocatalyst with the p–n heterojunction structure was prepared through ball milling. The morphologies, structures, and optical properties of the photocatalyst were comprehensively characterized. The transmission electron microscopy (TEM) images and the X-ray photoelectron spectroscopy (XPS) showed the interfacial interaction between g-C$_3$N$_4$ and Bi$_4$Ti$_3$O$_{12}$, indicating that a heterojunction between g-C$_3$N$_4$ and Bi$_4$Ti$_3$O$_{12}$ was formed during ball milling. In addition, the optimum activity of the coupling semiconductor is higher than that of individual g-C$_3$N$_4$ and Bi$_4$Ti$_3$O$_{12}$ for the degradation of acid orange-II(AO-7). The enhanced photocatalytic activity could be ascribed to the p–n junction of g-C$_3$N$_4$/Bi$_4$Ti$_3$O$_{12}$ with strong oxidative ability and efficient charge separation. The highest activity was obtained in the g-C$_3$N$_4$/Bi$_4$Ti$_3$O$_{12}$ p–n heterojunction using a composite of 10 wt.% g-C$_3$N$_4$ and 90 wt.% Bi$_4$Ti$_3$O$_{12}$ by ball milling in 16 h. The removal of AO-7 was not only mainly initiated by valence-band holes (h$^+$), but also affected by $^{\bullet}$O$_2$$^-$, which was verified by the effects of scavengers. The mechanism underlying the observed photocatalytic activity was also described based on the semiconductor energy band theory and the formation of an internal electrostatic field. The probable degradation pathways were proposed and discussed according to the primary degradation products identified by GC/MS.

© 2016 Elsevier B.V. All rights reserved.

1. Introduction

Photocatalysis for dealing with environmental problems such as water treatment, pollutant removal using solar light energy has attracted increasing interests for the past years due to the growing environment concerns and the energy demands [1–5]. Since TiO$_2$ was first implicated in the water splitting by Fujishima and Honda [6], the photocatalyic behavior of this compound in the degradation of organic dyes has been extensively studied. Although a photocatalyst titanium oxide has been recognized as the very important semiconductor in photocatalysis fields owing to its capacity to decompose a wide variety of pollutants and toxic substance [7], the large band gap of titania and massive recombination of photogenerated charge carriers limit its overall photocatalytic efficiency [8]. Therefore, much research has focused on developing the novel

photocatalysts with high photocatalytic properties [9–13]. Among these works, bismuth titanate (Bi$_4$Ti$_3$O$_{12}$, BTO), belonging to a family of layered perovskite compounds [14], has been highly concerned. Yao et al. [12,15] have reported the preparation of bismuth titanate (Bi$_4$Ti$_3$O$_{12}$) using the chemical solution decomposition (CSD) method and examined the photocatalytic property of Bi$_4$Ti$_3$O$_{12}$ crystals for photodegradation of methyl orange (MO). Furthermore, they have studied the factors affecting the photocatalytic activity of Bi$_4$Ti$_3$O$_{12}$, such as calcination condition for the photocatalyst, the pH value of the reaction suspension and so on. Hou et al. [14] have synthesized Bi$_4$Ti$_3$O$_{12}$ nanofibers by electrospinning with high activity for the photodegradation of rhodamine B (RhB). Nevertheless, some problems still remain to be solved, such as low capacity for the separation of photogenerated electron-hole pairs, the low activity in the visible light region and so on [12].

Graphitic carbon nitride (g-C$_3$N$_4$), a polymeric metal-free semiconductor with an indirect bandgap 2.7 eV [2], possesses outstanding thermal, electrical and optical characteristics [16]. These unique properties have aroused a lots of scientists' interest,

specially its potential applications in producing hydrogen or oxygen of water splitting and degrading organic pollutant [17–19]. However, the disadvantages of the pure g-C$_3$N$_4$, such as low quantum efficiency and the high recombination rate of its photogenerated electron–hole pairs, limit its photocatalytic efficiency [20,21].

An effective way to enhance the photocatalytic activity of catalyst is to construct heterojunction photocatalysts. As a promising method, heterojunction photocatalysts are of benefit to the separation of photogenerated electron-hole pairs, hence improving the photocatalytic properties [22–27]. Recently, heterojunction photocatalysts have been studied extensively [28–30]. The results have revealed that the photocatalytic activity of coupling photocatalyst is higher than that of the single one. Efficient charge separation can be reached by coupling two or more semiconductor photocatalysts.

Some studies show that *p–n* heterojunction photocatalysts have been paid much attention in the past several years, because *p–n* heterojunction makes for a facile separation of electron-hole pairs [31–35]. Kandjani et al. [35] have synthesized monodispersed Cu$_2$O nanocubes as the core, on which ZnO nanoparticles were coated as the shells having varying morphologies. This p-type Cu$_2$O/n-type ZnO core/shell composite has been demonstrated to be an efficient photocatalyst as a result of their interfacial structure tendency to reduce the recombination rate of photogenerated electron–hole pairs. He et al. [32] have prepared a novel visible-light-active BiOCl/BiVO$_4$ photocatalyst with a *p–n* heterojunction structure using a hydrothermal method, and revealed that the composite exhibited markedly improved efficiency for MO photodegradation in comparison with pure BiVO$_4$, BiOCl and Degussa P25. Hou et al. [33] have fabricated a novel *p–n* junction photocatalyst of Bi$_4$Ti$_3$O$_{12}$ nanofibers-BiOI nanosheets through a simple and economical technique of electrospinning combined with a successive ionic layer adsorption and reaction (SILAR) process, indicating that this *p–n* junction photocatalyst exhibited enhanced visible-light-driven photocatalytic activity for decomposition of RhB and phenol. Other *p–n* heterojunction photocatalysts have also been reported, such as *p*-Bi$_2$O$_3$/*n*-BiVO$_4$ [36], *p*-Cu$_2$O/*n*-TaON [37], *p*-CuFe$_2$O$_4$/*n*-Bi$_4$Ti$_3$O$_{12}$ [38] and *p*-Cu$_2$O/*n*-TiO$_2$ [23]. However, the preparation and properties of *p*-g-C$_3$N$_4$/*n*-Bi$_4$Ti$_3$O$_{12}$ heterojunction photocatalyst have not been investigated.

It is accepted that g-C$_3$N$_4$ and Bi$_4$Ti$_3$O$_{12}$ are intrinsic p-type and n-type semiconductor, respectively. Theoretically, when the p-type g-C$_3$N$_4$ and the *n*-Bi$_4$Ti$_3$O$_{12}$ integrate, a *p–n* junction will be formed between *p*-g-C$_3$N$_4$ and *n*-Bi$_4$Ti$_3$O$_{12}$, thereby the inner electric field will be formed in the interface. At the equilibrium, the inner electric field makes p-type semiconductor g-C$_3$N$_4$ region have the negative charge, while *n*-Bi$_4$Ti$_3$O$_{12}$ region have the positive charge. Under illumination, electron–hole pairs may be created, and the photogenerated electron–hole pairs are separated by the inner electric field. As a result, the photoexcited electrons and holes are separated efficiently, and the photocatalytic performance of this composite is enhanced.

Ball milling is a simple, effective and green (with no or minimal solvent) technique to synthesize composite photocatalysts [39]. Some studies have reported the use of a dry milling process while other studies have stated the use of a wet milling process(adding water as a dispersant) [40,41]. Zhao et al. have demonstrated that the effect of using a wet milling process (adding water as a dispersant) was better than a dry milling process [38].

In this work, we aimed at synthesizing the *p*-g-C$_3$N$_4$/*n*-Bi$_4$Ti$_3$O$_{12}$ heterojunction photocatalytic via ball milling with dispersant (H$_2$O). These composites were characterized by various techniques. The photocatalytic activity of the photocatalyst was evaluated by the photocatalytic degradation of acid orange II(AO-7). In addition, the possible mechanisms of *p–n* junction formation and separation of photoexcited electron and hole were investigated. The probable degradation pathways were proposed and discussed based on the degradation products identified by GC–MS.

2. Experimental

2.1. Materials

Acid orange II(AO-7), bismuth oxide (Bi$_2$O$_3$), titanium dioxide (TiO$_2$), melamine and other chemicals used in the experiments were of analytically pure grade (99%), without further purification. Deionized water was used throughout this study.

2.2. Preparation of photocatalysts

2.2.1. Preparation of g-C$_3$N$_4$ photocatalyst

Graphitic carbon nitride (g-C$_3$N$_4$) was synthesized according to a reported procedure [42]. In detail, 5 g melamine powder was put into an alumina crucible and calcined at 520 °C for 4 h with a heating rate of 5 °C/min, then calcined at 550 °C for another 3 h. After

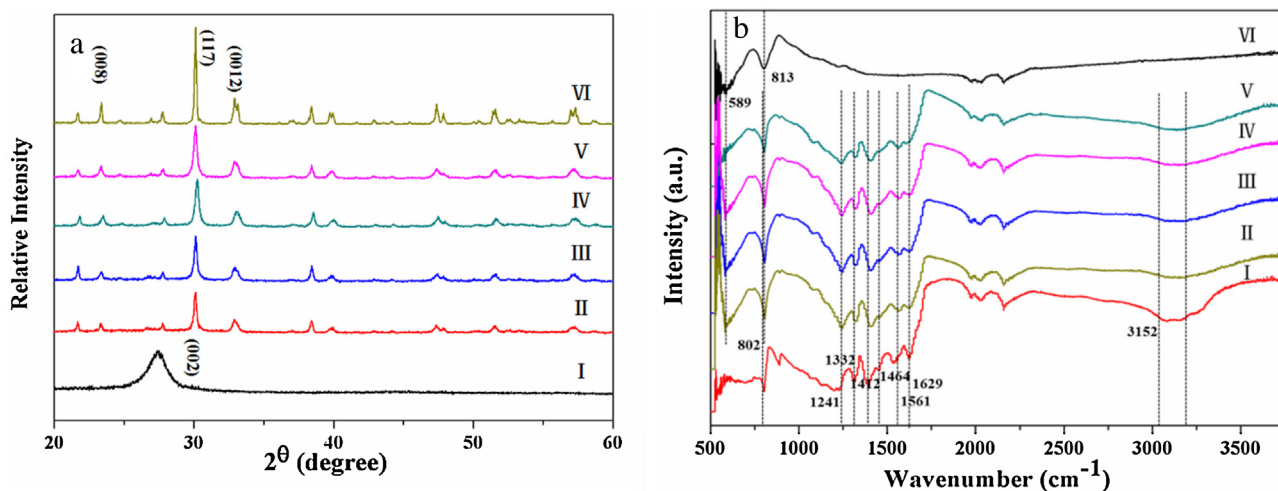**Fig. 1.** (a) XRD patterns of the photocatalysts: spectrum I: g-C$_3$N$_4$, spectrum II: N$_2$Bi$_{16}$, spectrum III: N$_5$Bi$_{16}$, spectrum IV: N$_{10}$Bi$_{16}$, spectrum V: N$_{20}$Bi$_{16}$ and spectrum VI: Bi$_4$Ti$_3$O$_{12}$. (b) FT-IR spectra of the photocatalysts: spectrum I: g-C$_3$N$_4$, spectrum II: N$_2$Bi$_{16}$, spectrum III: N$_5$Bi$_{16}$, spectrum IV: N$_{10}$Bi$_{16}$, spectrum V: N$_{20}$Bi$_{16}$ and spectrum VI: Bi$_4$Ti$_3$O$_{12}$.

Fig. 2. (a) XPS survey spectra of g-C₃N₄, Bi₄Ti₃O₁₂ and N₁₀Bi₁₆. High-resolution XPS spectra (b) C 1s of g-C₃N₄, Bi₄Ti₃O₁₂ and N₁₀Bi₁₆, (c) N 1s of g-C₃N₄ and N₁₀Bi₁₆, (d) O 1s of Bi₄Ti₃O₁₂ and N₁₀Bi₁₆ (e) Bi 4f of Bi₄Ti₃O₁₂ and N₁₀Bi₁₆ (f) Ti 2p of Bi₄Ti₃O₁₂ and N₁₀Bi₁₆.

cooling to room temperature, the received bulk g-C₃N₄ was milled into powders.

2.2.2. Preparation of Bi₄Ti₃O₁₂ photocatalyst

Briefly, Bi₂O₃ and TiO₂ with appropriate stoichiometric amounts were mixed well in alumina crucible, the mixture was calcined at 900 °C for 5 h with a temperature rise rate of 5 °C/min. After cal-

cination, the final products were cooled to room temperature and milled into powders.

2.2.3. Preparation of p-g-C₃N₄/n-Bi₄Ti₃O₁₂ photocatalyst

The preparation of the p–n heterojunction photocatalyst g-C₃N₄/Bi₄Ti₃O₁₂ was carried out in a QM-3SP04 ball miller (made

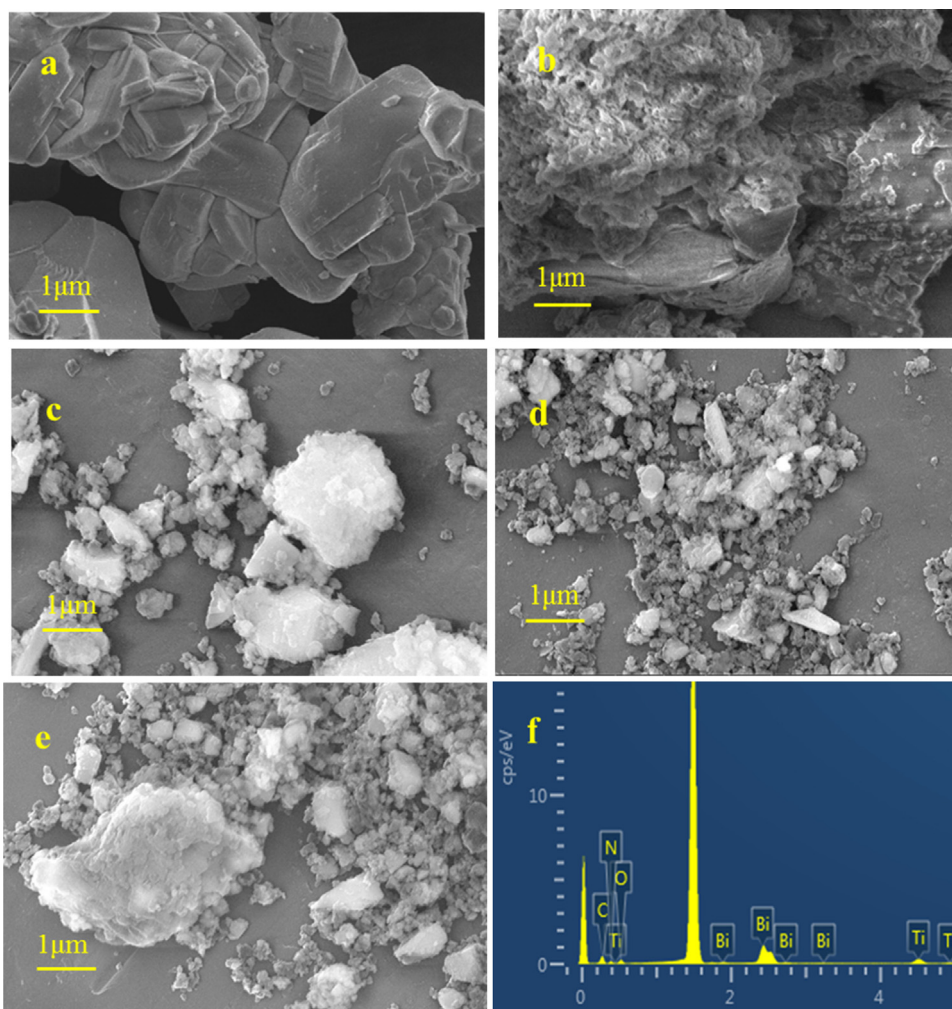**Fig. 3.** SEM images of the samples (a) $Bi_4Ti_3O_{12}$ without ball milling, (b) g-C_3N_4 without ball milling, (c) $N_{10}Bi_8$, (d) $N_{10}Bi_{16}$, (e) $N_{10}Bi_{24}$, (f) EDS spectrum of $N_{10}Bi_{16}$.

in Nanjing University). The details of the procedure were as follows: $Bi_4Ti_3O_{12}$ powders and the agate balls were mixed in the agate ball milling tank at a mass ratio of 1:10, a certain amount of g-C_3N_4 (2, 5, 10, 15 and 20 wt.%) and H_2O were subsequently added. After milling for a certain time (4, 8, 12, 16, 20 and 24 h) at a speed of 260 revolutions per minute (rpm), the samples were dried at 80 °C in a drying cabinet. The final samples were used for the investigation of photocatalytic performance and characterization. Briefly, the sample was denoted as N_aBi_b, in which N and Bi represent g-C_3N_4 and $Bi_4Ti_3O_{12}$, respectively, and the subscript a and b represent the amount of g-C_3N_4 in weight percent (wt.%) and the time of ball milling in hours.

2.3. Characterization of photocatalysts

X-ray diffraction (XRD) was conducted on a XRD-6000 X-ray powder diffractometer (Shimadzu) with monochromatic Cu-Kα radiation at a setting of 40 kV and 30 mA. The FT-IR spectra of the as-prepared samples were recorded on a Nicolet iS10 FT-IR instrument within the IR range (500–4000 cm^{-1}).

A PHI 5000 Versa Probe spectrometer (ULVAC-PHI, Japan) with monochromatized Al-Kα radiation was used for the X-ray photoelectron spectroscopy (XPS) analysis and the binding energy positions were calibrated against the C1s at 284.6 eV.

The morphology characteristics of the photocatalysts were investigated via scanning electron microscopy (SEM) and transmis-

sion electron micrographs (TEMs).The SEM images were taken on QUANTA FEG 250. Transmission electron micrographs (TEMs) were carried out on a JEM-200CX instrument.

UV–vis diffuse reflectance spectroscopy (DRS) was performed on a UV-3600 spectrophotometer equipped with an integrating sphere attachment at room temperature in a wavelength range of 200–800 nm.

Fluorescence emission spectra and time-resolved fluorescence measurements were recorded over a wavelength range of 340–800 nm on a Horiba Fluorolog 3–22 type fluorescence spectrophotometer with excitation wavelength of 320 nm.

The photoelectrochemical characterization was conducted on a CHI760E electrochemical workstation (Shanghai, China) with a standard three-electrode system. The prepared samples were loaded onto ITO electrode (1 cm × 2 cm squares) and served as the working electrode. Pt plate and Ag/AgCl electrode were used as the counter and reference electrodes, respectively. The electrolyte was 0.2 M Na_2SO_4 aqueous solution. A 500 W xenon lamp was employed to provide light source.

The Brunauer–Emmett–Teller (BET) surface areas were determined using a Micromeritics ASAP 2010 N_2 adsorption apparatus

2.4. Photocatalytic activity

The photocatalytic activities of as-synthesized photocatalysts were evaluated by catalytic degradation of acid orange II(AO-
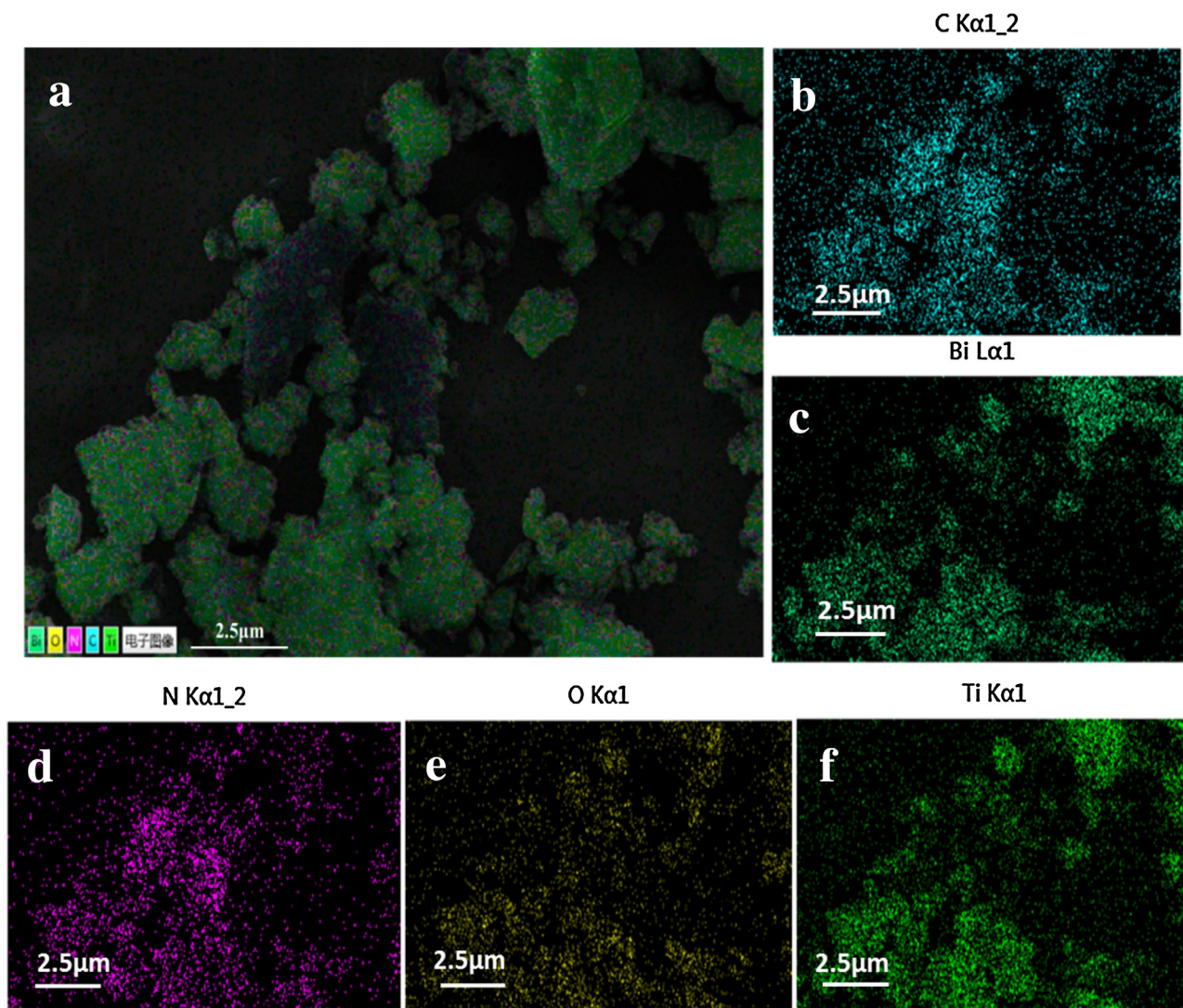
Fig. 4. (a) FESEM-EDS mapping of $N_{10}Bi_{16}$, (b)–(f) FESEM-EDS elemental mappings of C, Bi, N, O, Ti.

7)under visible light irradiation in a photoreaction apparatus (XPA-V, Xujiang, China, Nanjing). A 500 W xenon lamp with a 420 nm cut-off filter to remove light of $\lambda < 420$ nm was used as the visible light source. In a typical experiment, the reactant and the catalysts were placed in quartz tube. Prior to light illumination, the suspension was magnetically stirred for 60 min in the dark to reach adsorption–desorption equilibrium. At given time intervals after initiation of visible light irradiation, the samples (volume of each is 4 mL) were taken from the reaction suspension, centrifuged at 7000 rpm for 10 min and filtered through a 0.22 μm Millipore filter to remove the particles. Then, the concentration of AO-7 in solution was analyzed using a Lambda 750 UV–vis spectroscopy (PerkinElmer) at its maximum absorbance wavelength. To ensure the reproducibility of the results, duplicate runs were performed to obtain averaging data for each condition. A blank test was also performed through the irradiation of reactant solution without catalyst to assess photoinduced self-sensitized photodegradation.

2.5. Analytical methods

The concentration of the targeted compound was determined using a UV–vis spectrophotometer. The photocatalytic degradation efficiency was calculated by the followingexpression:

$$\eta = \frac{C_0 - C_t}{C_0} \times 100\%$$

Where η is the photocatalytic efficiency; C_0 is the concentration of reactant before illumination; C_t is the concentration of reactant after illumination of t hours.

The degradation products of AO-7 were analyzed by gas chromatography–mass spectrometer (GC–MS). Prior to GC–MS analysis, the aqueous samples (50 mL) were centrifuged and filtered through 0.22 μm Millipore filter to remove agglomerates in suspension. Then the samples were extracted with dichloromethane (15 mL) for three times. The extracted solution was dehydrated using anhydrous sodium sulfate and concentrated to about 1 mL by rotary evaporation. Trimethylsilylation was carried out at 60 °C for 2 h using 100 μL of bis(trimethylsilyl)trifluoroacetamide (BSTFA).

The GC was equipped with an TG-5SILMS column($30\,m \times 0.25\,mm \times 0.25\,\mu m$) The temperature program of GC operation was as follows: an initial temperature of the column oven was 60 °C, accordingly increased up to 100 °C with a heating rate of 12 °C/min and then to 200 °C with 5 °C/min, where it was held for 2 min, finally ramped to 280 °C with a 10 °C/min rate and held at that temperature for 5 min. Helium was used as the
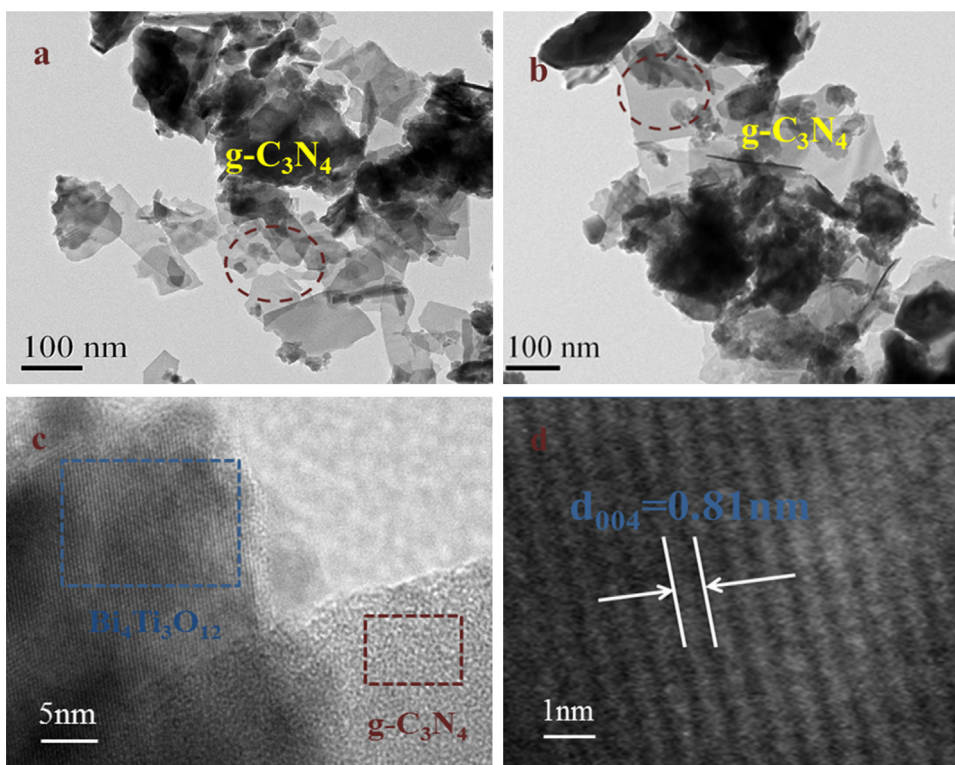
Fig. 5. (a) and (b) TEM images of the sample $N_{10}Bi_{16}$; (c) and (d) HRTEM images of the sample $N_{10}Bi_{16}$.

carrier gas. Mass spectrometric detection was operated with 70 eV electron impact (EI) mode.

3. Results and discussion

3.1. Morphology and structure

3.1.1. XRD analysis

XRD was used to determine the phase structures of the as-prepared samples. Fig. 1a shows the XRD patterns of photocatalysts ball-milled for 16 h. It can be indexed that the pattern of as-prepared pure $Bi_4Ti_3O_{12}$ sample can be well matched to the XRD peaks of pure orthorhombic $Bi_4Ti_3O_{12}$ (JCPDS 12–213). The 2θ diffraction peaks of 23.3°, 30.1°, 32.8° can be respectively indexed as (008), (117), (0012) planes of orthorhombic $Bi_4Ti_3O_{12}$ structure. The sharp and intense diffraction peaks of the samples indicate that the pure $Bi_4Ti_3O_{12}$ is a highly crystalline nature. One pronounced peak is found in g-C_3N_4 at 27.4°, which can be indexed to (002) diffraction planes of the graphite-like carbon nitride (JCPDS 87–1526). For the g-C_3N_4/$Bi_4Ti_3O_{12}$, the diffraction peaks of g-C_3N_4 could not be determined from the XRD patterns, suggesting that g-C_3N_4 is highly dispersed during the bulk phase of the sample. Therefore, ball milling is an effective way to make the samples efficiently mill with high dispersion so that the diffraction peaks of the g-C_3N_4/$Bi_4Ti_3O_{12}$ become smoother and wider, comparing to the diffraction peaks of pure g-C_3N_4 and pure $Bi_4Ti_3O_{12}$. Since no new crystal phases are found, it can be concluded that a new substance is not formed in the ball milling process of g-C_3N_4 and $Bi_4Ti_3O_{12}$.

3.1.2. FT-IR analysis

To further observe the existence of g-C_3N_4 and the effect of the hybrid combination, FT-IR was carried out (Fig. 1b). In the case of the pure $Bi_4Ti_3O_{12}$, the broad band centered at 589 cm^{-1} and the band at 813 cm^{-1} are contributed to the stretching vibrations of Bi–O and Ti–O, respectively [43,44]. From the spectrum of the pure g-C_3N_4,

it can be seen that absorption peak at 805 cm^{-1} corresponds to s-triazine ring modes [45]. Absorption bands at 1200–1700 cm^{-1} are mainly due to the typical stretching modes of CN heterocycles [17]. In addition, the peak observed at 3152 cm^{-1} is mostly ascribed to N—H stretching vibration [46], which is present in the g-C_3N_4/$Bi_4Ti_3O_{12}$ composites with the increasing content of g-C_3N_4. The intensity of these peaks decreases, which reveals that g-C_3N_4 exists in the obtained composite.

3.1.3. XPS analysis

XPS spectra are used to reveal the surface chemical composition of $N_{10}Bi_{16}$ and the interaction between g-C_3N_4 and $Bi_4Ti_3O_{12}$ in the composite. Fig. 2 displays the survey of g-C_3N_4, $Bi_4Ti_3O_{12}$ and $N_{10}Bi_{16}$ and high-resolution XPS spectra of the C 1s, N 1s, O 1s, Bi 4f and Ti 2p for these three samples. The survey spectra indicate that C and N exist on the surface of g-C_3N_4, Bi, Ti, O and C on the surface of $Bi_4Ti_3O_{12}$, and C, N, Bi, Ti and O on the surface of $N_{10}Bi_{16}$. As shown in Fig. 2b, C 1s peak at about 284 eV can be assigned the adventitious carbon depositing on the surface of photocatalyst [17,47]. In the case of g-C_3N_4, the major peak of C 1s at 287.4 eV is attributed to coordination between carbon atoms and three nitrogen atoms in the g-C_3N_4 lattice [48]. The asymmetrical N 1s peaks in Fig. 2c can be fitted into three peaks located at 398.2, 399.6 and 400.2 eV, indicating three different kinds of N species in the sample. The peaks with lower binding energy located at about 398.2 and 399.6 eV, corresponding to pyridinic-like (N-sp^{2}C) and pyrrolic-like (N-sp^{3}C) nitrogen, while the peak centered at 400.2 eV corresponds to graphitic nitrogen [49]. Compare to the g-C_3N_4, the peak positions of C 1s and N 1s in sample $N_{10}Bi_{16}$ shift to higher binding energies. It is also observed that a similar result was obtained for binding energies of O 1s, Bi 4f and Ti 2p.

Three peaks with binding energies of 529.1, 530.9 and 531.5 eV are observed in the high-resolution O1s spectra of pure $Bi_4Ti_3O_{12}$ (Fig. 2d). The primary peak at 529.1 eV is attributed to the lattice oxygen O^{2-} (in the stronger Bi—O band), the secondary one at
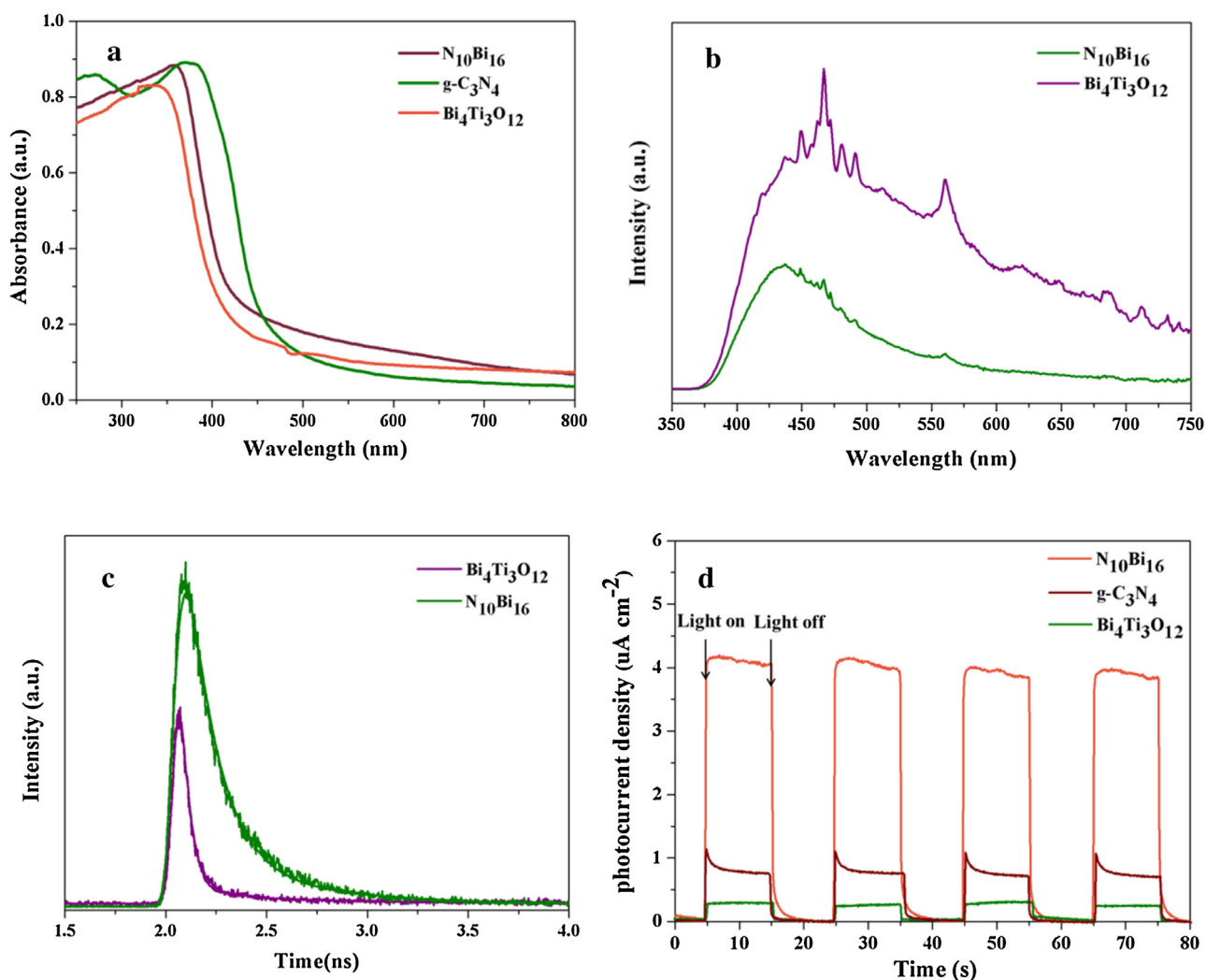
Fig. 6. (a) UV–vis diffuse reflectance spectra of pure g-C$_3$N$_4$ and pure Bi$_4$Ti$_3$O$_{12}$, N$_{10}$Bi$_{16}$, (b) fluorescence emission spectra of different samples Bi$_4$Ti$_3$O$_{12}$ and N$_{10}$Bi$_{16}$, (c) time-resolved fluorescence decay observed at 460 nm of the corresponding samples Bi$_4$Ti$_3$O$_{12}$ and N$_{10}$Bi$_{16}$ following 320 nm laser excitation. (d) Photocurrents of pure g-C$_3$N$_4$, pure Bi$_4$Ti$_3$O$_{12}$ and N$_{10}$Bi$_{16}$ electrodes under visible light irradiation ($\lambda > 450$ nm).

530.9 eV is assigned to the Ti—O band in Bi$_4$Ti$_3$O$_{12}$. The third one at a higher bonding energy of 531.5 eV is ascribed to surface adsorbed oxygen (–OH group and chemisorbed oxygen-containing species) [33]. These peaks in N$_{10}$Bi$_{16}$ shift to 529.6, 531.4 and 532 eV. Fig. 2e shows the high-resolution XPS spectrum of Bi 4f of Bi$_4$Ti$_3$O$_{12}$, in which peaks of 159.4 eV and 164.7 eV are observed [14]. Those peaks are attributed to Bi 4f$_{5/2}$ and Bi 4f$_{7/2}$ of Bi^{3+}, respectively [50]. The peaks of Bi 4f$_{5/2}$ and Bi 4f$_{7/2}$ in N$_{10}$Bi$_{16}$ were also shifted up by 0.5 eV. In the fitting result of Ti 2p (Fig. 2f), the peaks of Ti 2p$_{1/2}$ and Bi 4d$_{3/2}$ are partially overlapped, leading to a broad crest in the vicinity of 465.0 eV. The Ti 2p$_{3/2}$ and Ti 2p$_{1/2}$ peaks with a typical spin orbit doublet of 5.7 eV are at 457.1 and 462.8 eV, respectively, which are characteristic of Ti(IV) [33]. Compared to pure Bi$_4$Ti$_3$O$_{12}$, the observed Ti 2p peaks of N$_{10}$Bi$_{16}$ also shifted to higher binding energies. These results could be attributed to the interaction between the Bi$_4$Ti$_3$O$_{12}$ and g-C$_3$N$_4$ [51].

3.1.4. SEM and EDS analysis

The morphology and structure of the as-prepared g-C$_3$N$_4$, Bi$_4$Ti$_3$O$_{12}$, g-C$_3$N$_4$/Bi$_4$Ti$_3$O$_{12}$ were investigated by SEM. Fig. 3a and 3b demonstrate the SEM photographs of the Bi$_4$Ti$_3$O$_{12}$ and g-C$_3$N$_4$ powders, respectively, without ball milling. The photograph of Bi$_4$Ti$_3$O$_{12}$ shows various small block aggregations of particles distributing in irregular shapes. Fig. 3b shows that the bulk g-C$_3$N$_4$ sample is comprised of the accumulation of flakes.

Fig. 3c–e shows the SEM images of N$_{10}$Bi$_8$, N$_{10}$Bi$_{16}$, N$_{10}$Bi$_{24}$, respectively. The sizes of these aggregations decrease as the milling time increases in comparison to the samples without ball milling. The milling of 16 h makes the resulting powders dispersed well. It clearly indicates that the successful production of well-dispersed samples through ball milling. However, when the ball milling time is 24 h, the aggregation degree of the sample is slightly higher than that at 16 h. Thus, when the ball milling time is longer than the optimum time, the fresh surfaces are formed through high-energy ball milling with the increase of the milling time, which results from their high surface energy to lead to gradually agglomerate, and to decrease the specific surface area of the sample.

EDS of the sample N$_{10}$Bi$_{16}$ was also performed to study the composition of the sample(Fig. 3f). The EDS image verifies that the sample is composed of the elements of C, N, Ti, O and Bi. The highest peak is the background peak of carbon conductive adhesive tape used during the preparation of EDS sample. Moreover, the FESEM-EDS mappings intuitively express the distribution of corresponding elements in the composite catalyst. The FESEM-EDS mappings of the sample N$_{10}$Bi$_{16}$ and the corresponding elements are exhibited in Fig. 4. These images suggest the co-existence of g-
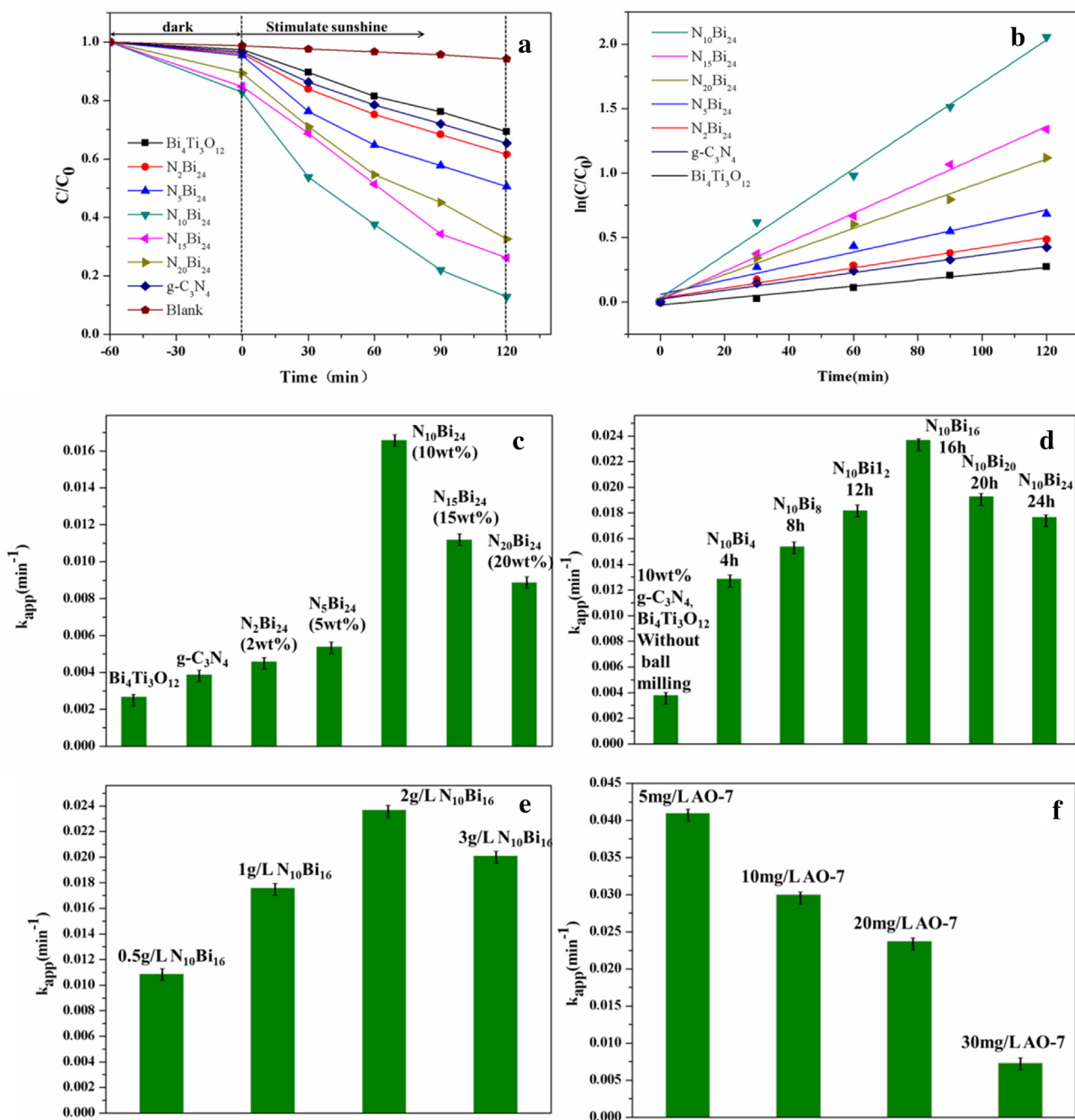
Fig. 7. (a) Degradation of AO-7 over sample with different amounts of doped g-C_3N_4, (b) pseudo-first-order kinetics curves of AO-7 degradation over different samples. Effects of (c) g-C_3N_4 content, (d) ball milling time, (e) photocatalyst amount in the degradation of 20 mg/L AO-7, and (f) initial AO-7 concentration on the photocatalysis with $N_{10}Bi_{16}$ photocatalyst.

C_3N_4 and $Bi_4Ti_3O_{12}$. It can be seen that the elements such as C, N, Ti, O and Bi are uniformly distributed in the composite.

3.1.5. TEM and HRTEM analysis

The morphology and microstructural details of the sample $N_{10}Bi_{16}$ were investigated by TEM and HRTEM observation. Fig. 5a and b show the overview of the typical TEM image of the sample. The image clearly indicates the existence of g-C_3N_4 dispersed over the $Bi_4Ti_3O_{12}$. Moreover, the bulk g-C_3N_4 with ball milling is turned into the one with structure of flake, coinciding with the results from SEM images. HRTEM images of the sample display two types of lattice in Fig. 5 c and d. A clear interface is observed in Fig. 5c. The

HRTEM images in Fig. 5d was obtained from blue square regions. Fig. 5d clearly exhibits the $Bi_4Ti_3O_{12}$ (004) facet with a spacing of 0.81 nm. The perfect crystalline quality and the clear interface between g-C_3N_4 and $Bi_4Ti_3O_{12}$ would facilitate the separation of the photo-excited charge carriers.

3.2. Optical properties

3.2.1. UV–vis analysis

In order to investigate the changes in optical properties caused by the loaded g-C_3N_4, the samples were analyzed by UV–vis diffuse reflectance spectroscopy. Fig. 6a illustrates that after the incorpo-
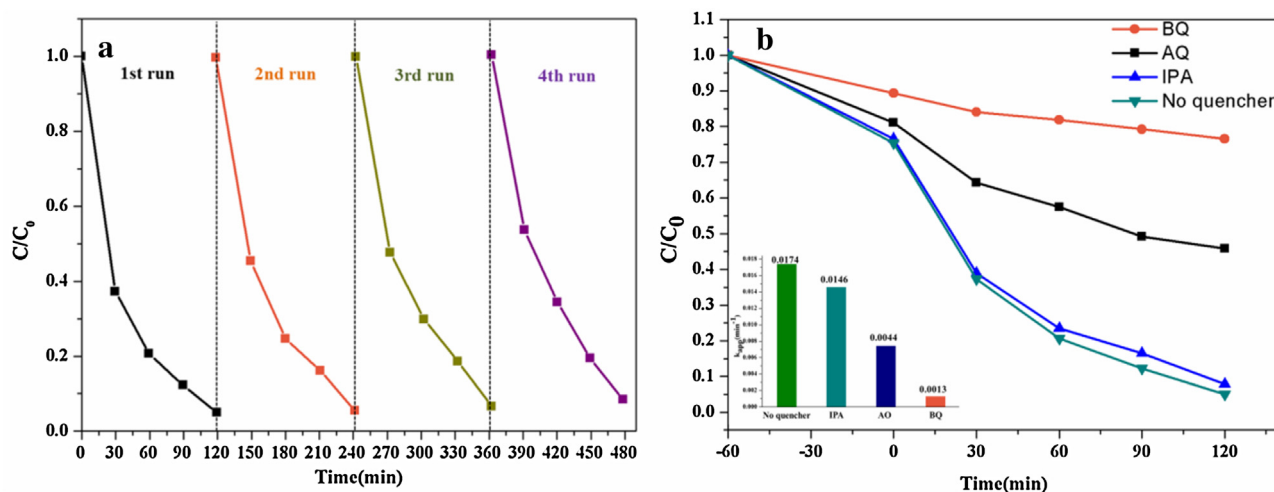
Fig. 8. (a) Cycling run in the photocatalytic degradation of AO-7; (b) photocatalytic activity of $N_{10}Bi_{16}$ for AO-7 with different scavenges under visible light irradiation.

ration of $g-C_3N_4$, the optical absorption of the composites in the visible region increases, indicating the composite should possess better visible light photocatalytic performance. In addition, the band gap energy (Eg) of the samples calculated according to the following Eq. (1):

$$\alpha h\nu = A(h\nu\text{-}Eg)^n \qquad (1)$$

Where α, $h\nu$, A and Eg signify the absorption coefficient, photo energy, proportionality constant and band gap, respectively. The index n depends on the electronic transition of the semiconductor, n = 1/2 for direct-gap semiconductor and n = 2 for indirect-gap semiconductor. For $g-C_3N_4$ and $Bi_4Ti_3O_{12}$, n equals 1/2 and 2 separately [33,52]. By extrapolating the linear portion of $(\alpha h\nu)^{1/2}$ versus $(h\nu)$ curves and $(\alpha h\nu)^2$ versus $(h\nu)$ curves, the Egs of $Bi_4Ti_3O_{12}$ and $g-C_3N_4$ are estimated to be about 2.84 eV, 2.68 eV in Fig. S1a and b, respectively, which is consistent with literature [33,53].

3.2.2. Photoluminescence spectra

The recombination of the photo-induced electrons and holes will decrease the activity of a photocatalyst. The photoluminescence spectra of the semiconductor are useful to disclose the migration, transfer, and recombination processes of the photogenerated electron-hole pairs. After being activated by light, photocatalysts generate electrons and holes, while recombination of some electrons and holes can release energy in the form of fluorescence emission. Lower fluorescence emission intensity implies lower recombination rate of electron–hole [54,55]. The fluorescence emission spectra of the samples excited at a wavelength of 320 nm are shown in Fig. 6b, the emission spectrum of $Bi_4Ti_3O_{12}$ shows a relatively high intensity, indicating that electrons and holes of $Bi_4Ti_3O_{12}$ are easily recombined. The intensity of the PL peak for $N_{10}Bi_{16}$ heterojunction photocatalyst is lower than that of pure $Bi_4Ti_3O_{12}$. Thus, the result indicates that $N_{10}Bi_{16}$ heterojunction photocatalyst may be greatly improved, compared with pure $Bi_4Ti_3O_{12}$.

To clarify the separation of photoexcited charge carriers, we obtained the ns-level time-resolved fluorescence decay spectra for $Bi_4Ti_3O_{12}$ and $N_{10}Bi_{16}$ in Fig. 6c. The experimental curves are fit according to $f(t) = B + A_1 \times \exp(-t/\tau_1) + A_2 \times \exp(-t/\tau_2)$, The lifetimes ($\tau_1$ and τ_2), pre-exponential factors (A_1 and A_2), and average lifetime τ_{avg} of samples are summarized in Table 1. In details, the average decay lifetime of carriers in the sample $N_{10}Bi_{16}$ is 3.238 ns, relatively slow compared with pure $Bi_4Ti_3O_{12}$ (0.219 ns). The greatly prolonged lifetime of the charge carriers indicates that a lower recombination and a higher separation of charge car-

Table 1
Summary of time-resolved fluorescence decay data of the corresponding samples.

Samples	T_1	A_1	T_2	A_2	T_{avg}
$Bi_4Ti_3O_{12}$	0.169	0.358	11.235	0.00163	0.219
$N_{10}Bi_{16}$	1.809	0.0457	7.231	0.00427	3.238

riers exist in the composite catalyst [56]. This high separation efficiency could improve the probability of their involvement in photocatalytic reaction before recombination and thus enhance the photocatalytic activity [57].

3.2.3. Photocurrent

Photocurrent test was performed to investigate the photoresponse of the samples. The value of photocurrent indirectly reflects the semiconductor's ability of generating and transferring of photogenerated charge carriers under irradiation [58]. As comparatively studied in Fig. 6d, the photocurrent decreases with the order of $N_{10}Bi_{16} > g-C_3N_4 > Bi_4Ti_3O_{12}$. The maximum photocurrent density of $N_{10}Bi_{16}$ is nearly 8 times higher than that of pristine $Bi_4Ti_3O_{12}$. It presents the positive effect of $g-C_3N_4$ on increasing the photocurrent density. Moreover, this enhancement on the photocurrent density demonstrates higher separation efficiency of photogenerated charge carriers in $N_{10}Bi_{16}$ composite.

3.3. Evaluation of photocatalytic activity

3.3.1. Effect of the amount of loaded $g-C_3N_4$ on the photocatalytic activity

To evaluate the photocatalytic activity of the as-prepared samples, the photodegradaion of AO-7 in water was investigated under visible light irradiation in the present study. A dark adsorption experiment was carried out for 60 min to achieve an equilibrium adsorption state. Moreover, photolysis of AO-7 without the photocatalyst as the reference experiments was also investigated.

Fig. 7a illustrates the effects of amount of loaded $p-C_3N_4$ on the photocatalytic degradation of AO-7. The amount of photocatalyst and the initial concentration of AO-7 used in experiment are 2.0 g/L and 20 mg/L, respectively. The results demonstrate that the photocatalytic activity of the coupling of $n-Bi_4Ti_3O_{12}$ with $p-g-C_3N_4$ is significantly superior to pure $Bi_4Ti_3O_{12}$ and $g-C_3N_4$. Furthermore, $N_{10}Bi_{24}$ exhibits the highest photocatalytic activity among the as-prepared samples. From Fig. 7a, the photodegradation of AO-7 over pure $Bi_4Ti_3O_{12}$ is 30.6% after 120 min of light irradiation. However, the degradation rate (87.2%) of AO-7 is obtained within 120 min

Table 2
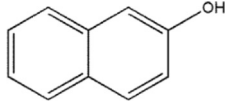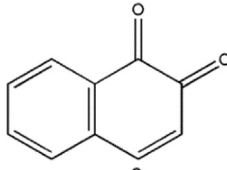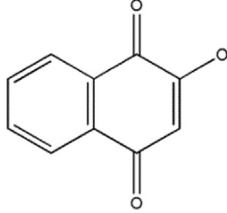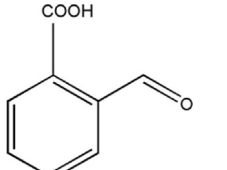Identification of the degradation intermediates of AO-7 by GC–MS.

Product	Retention time (min)	m/z	Name	Molecular structure
A	18.79	144	β-Naphtalenol	
B	21.65	158	1,2-naphtraquinone	
C	33.48	174	2-hydroxy-1,4-naphthalenedione	
D	22.9	150	2-formyl-benzoic acid	
E	10.74	138	Salycilic acid	
F	14.96	148	o-Phthalic anhydride	
G	37.34	174	4-hydroxbenzenesulphonic acid	
H	8.88	111	Hydroquinone	
I	7.82	108	1,4-benzoquinone	
J	19.69	150	2,3-dihydroxybutanedioic acid	

Table 2 (*Continued*)

Product	Retention time (min)	*m/z*	Name	Molecular structure
K	9.05	116	Maleic acid	
L	6.21	60	Acetic acid	
M	6.95	60	Glycolaldehyde	
N	7.27	74	Propionic acid	

Fig. 9. Crystal structures, calculated band structures and density of states of $Bi_4Ti_3O_{12}$ (a, b) and g-C_3N_4 (c, d).

of photocatalysis by the sample $N_{10}Bi_{24}$. Therefore, the optimum amount of loaded p-g-C_3N_4 is 10 wt.%. When the amount of loaded g-C_3N_4 increases higher than the optimal amount, the photocatalytic activity of g-C_3N_4/$Bi_4Ti_3O_{12}$ decreases. When the amount of loaded g-C_3N_4 achieves 20 wt.%, the photocatalytic activity reduces to 67.3%, which is obviously less than that of the sample $N_{10}Bi_{24}$.

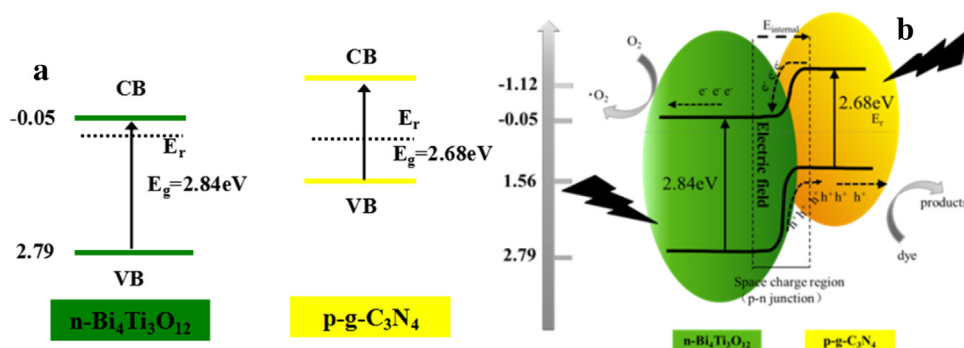**Fig. 10.** Schematic illustrations of the energy band structures (a) for separate phases and (b) after the formation of $Bi_4Ti_3O_{12}$ and $g-C_3N_4$ $p–n$ heterojunction.

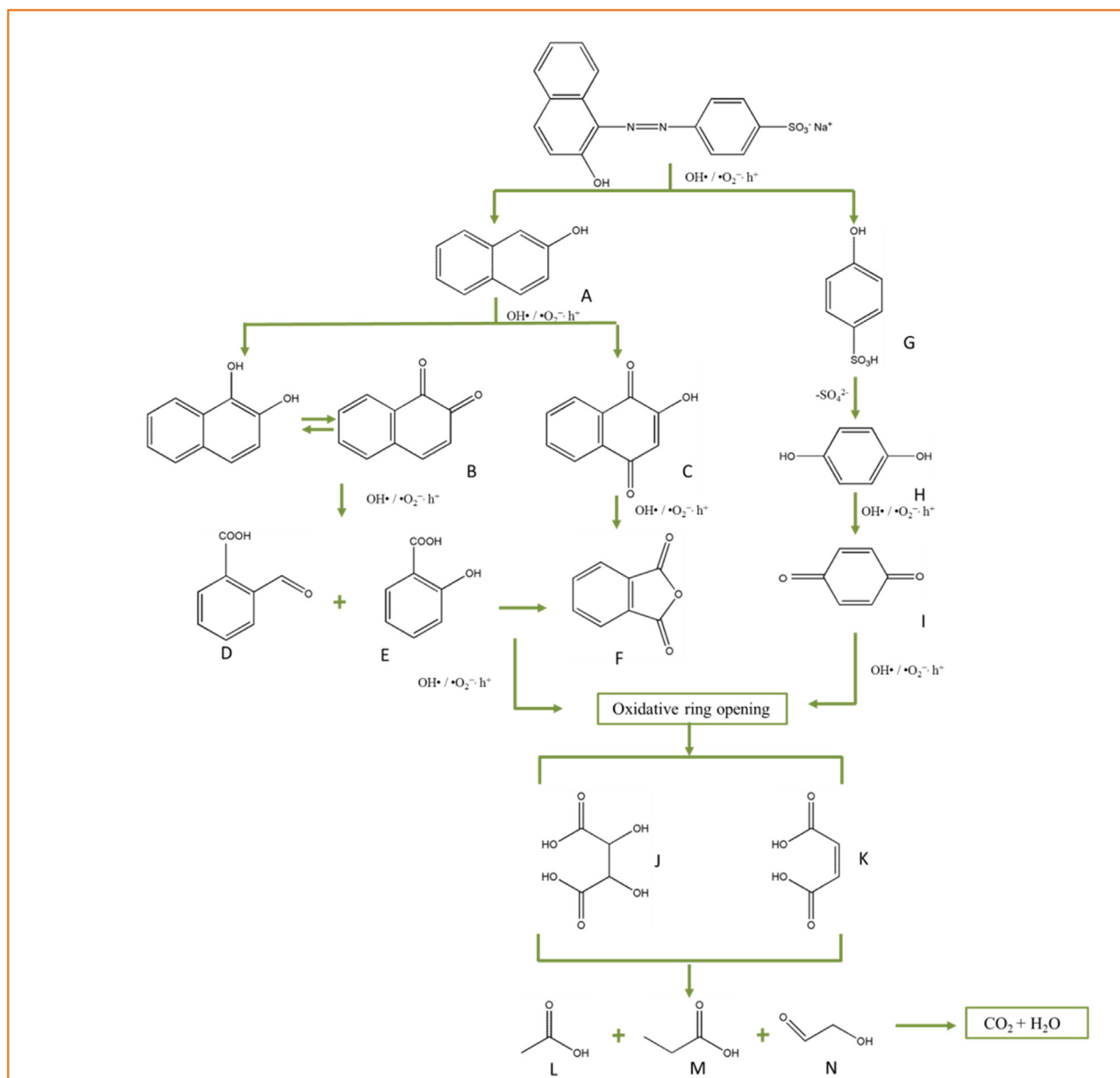**Fig. 11.** Proposed AO-7degradation pathways on the $N_{10}Bi_{16}$.

Following the Langmuir−Hinshelwood model, the apparent reaction rate constants of the photocatalytic degradation of organic pollutants in aqueous suspensions could be obtained from Eq. (2) [59]:

$$\ln(C_0/C) = k_{app}t \tag{2}$$

Where C is the concentration of AO–7 at time t, C_0 is the initial concentration of AO-7 solution, and the slope k is the apparent reaction rate constant. From the linear time dependence of ln (C_0/C), the first-order rate constant k_{app} could be obtained [60]. The greater the reaction rate constant, the better the photocatalytic activity [61]. Based on the curves from Fig. 7b, the calculated values of k_{app} are displayed in Fig. 7c. It is clear that, $N_{10}Bi_{24}$ has the highest k_{app} value and corresponds to the best photocatalytic activity; whereas the k_{app} of pure $Bi_4Ti_3O_{12}$ is the lowest. The k_{app} of $N_{10}Bi_{24}$ (0.0167 min^{-1}) is approximately 6 times than that of the pure $Bi_4Ti_3O_{12}$ (0.0024 min^{-1}). The results reveal that the amount of g-C_3N_4 plays an important role in the property of the photocatalyst. It has proposed that as the amount of g-C_3N_4 increases until reaching the optimum value, the trapping sites of carriers increase, which could prolong the lifetime of carriers, thereby improving the photocatalytic performance. In addition, the photocatalytic performance increases due to the formation of p–n heterojunction between g-C_3N_4 and $Bi_4Ti_3O_{12}$ through ball milling. However, when the amount of g-C_3N_4 is higher than the optimum amount, the photocatalytic performance could be reduced. This might attribute to the high amount of g-C_3N_4 which acts as a recombination center for electrons and holes. Accordingly, excess g-C_3N_4 might not effectively form the p–n heterojunction photocatalyst [62].

3.3.2. Effect of ball milling on the photocatalytic activity

The k_{app} values of the as-prepared samples were calculated to illustrate the effect of ball milling on the photocatalytic activity of g-C_3N_4 (10 wt.%)/$Bi_4Ti_3O_{12}$ photocatalyst in Fig. 7d. The results show that the ball milling time affects photocatalytic activity strongly. When the sample is ball-milled for 4, 8, 12, 16, 20 and 24 h, the k_{app} values are 0.0166, 0.0177, 0.0193, 0.0237, 0.0138 and 0.0129 min^{-1}, respectively. Without ball milling, the k_{app} of the sample is 0.0038 min^{-1}. The k_{app} of the sample gradually ascends as the ball milling time increases up to 16 h, however, as the time increases more than 16 h, there's no proliferation for the k_{app} value, which demonstrates that the optimum ball milling time is 16 h.

Without ball milling, g-C_3N_4 and $Bi_4Ti_3O_{12}$ play separate photocatalytic roles, as heterojunction is not formed. During the ball milling, the heterojunction between $Bi_4Ti_3O_{12}$ and g-C_3N_4 is formed, resulting in increased photocatalytic activity. Additionally, when the ball milling time increases, the particle size of the photocatalyst decreases, which leads to an additional number of active sites per unit weight of photocatalyst. Nevertheless, the particle size has no significantly change when the ball milling time is longer than the optimum time. Indeed, beyond the optimum time (16 h) among the experiment, the fresh surfaces form through high-energy ball milling which possess high surface energy and tend to slightly agglomerate [63]. Consequently, the photodegradation activity gradually reduces compared with the sample milled with optimum time.

3.3.3. Effect of amount of photocatalyst on the photocatalytic activity

The amount of photocatalyst is one of critical parameters for the degradation efficiency of targeted organic compounds. In this study, a series of experiments were conducted with varying photocatalyst amount from 0.5 to 3.0 g/L, at dye concentration of 20 mg/L. The corresponding k_{app} values of the compound degradation were calculated to be presented in Fig. 7e, illustrating that the k_{app} value of the sample increases from 0.123 to 0.162 min^{-1} as the amount of

photocatalyst increases from 0.5 to 2 g/L after 120 min irradiation. The highest value of 0.0162 min^{-1} is achieved at 2.0 g/L of photocatalyst. It has been considered that the photon absorption and the active sites of the samples greatly influence dye degradation. The increase in the catalyst amount contributes to the proliferation in the number of photons absorbed and the number of the dye molecules adsorbed [64]. But the further increase in the sample amount beyond 2.0 g/L does not have an obvious positive effect on the degradation of AO-7. This is because higher photocatalyst amount implying more active sites can absorb much more photons. The excess amount of the photocatalyst might enhance the light reflectance and light blocking, thus obtaining decreases of light penetration and light scattering [65]. Therefore, 2 g/L is used as the optimal catalyst amount for photocatalytic reaction.

3.3.4. Effect of initial AO-7 concentration on the photocatalytic activity

The effect of different initial AO-7 concentrations on the efficiency of photocatalytic degradation was investigated in the presence of the 2.0 g/L catalyst. As shown in Fig. 7f, the k_{app} values of AO-7 decrease from 0.0410 to 0.0073 min^{-1} with an increase in the initial AO-7 concentration from 5 to 30 mg/L. The reason is because the dye affects the visible light screening. High AO-7 concentration may absorb a significant amount of visible light, which shields the light absorption for catalyst. Undoubtedly, it should be a hindrance for the photocatalyst to utilize the light and to reduce the photocatalytic activity of the sample.

3.3.5. Stability of the catalyst

The lifetime of the photocatalyst is a major parameter for the catalytic process. The results for the stability and the reusability of the p–n heterojunction photocatalyst $N_{10}Bi_{16}$ during photocatalytic degradation are shown in Fig. 8a. It can be seen that the photocatalytic degradation was 95.1% at the first cycling run, and was 91.9% after the fourth cycling run. Thus, the sample exhibits adequate stability without remarkable reduction of photocatalytic activity.

3.4. Discussion of the underlying mechanism of photocatalysts

3.4.1. Roles of reactive species

Photocatalytic oxidation usually happens during the photodegradation of the dyes and organic pollutants [23,66]. In the photocatalytic process, the main oxidative species $^\bullet$OH, $^\bullet$O$_2^-$ and h$^+$ can be detected by adding benzoquinone (BQ), ammonium oxalate (AO) and isopropanol (IPA) into the photocatalytic reaction systems [67,68]. This is crucial for elucidating the photocatalytic mechanism. The comparative experiment with no quencher was also performed under identical conditions. As a result of quenching, reaction will be partially suppressed and k_{app} will decrease. The more the k_{app} value decreases through the activity of scavengers, the more important the role of the corresponding oxidizing species in the photodegadation process.

As shown in Fig. 8b, different scavengers have different effects on the degradation of AO-7 over the $N_{10}Bi_{16}$ heterojunction system. The addition of $^\bullet$OH quencher induces a little change in AO-7 photodegradation, as the k_{app} value has no obviously reduced. However, the photocatalytic activity of the $N_{10}Bi_{16}$ heterojunction is suppressed by addition of h$^+$ or $^\bullet$O$_2^-$ quencher, as the k_{app} values obviously decrease, suggesting that $^\bullet$O$_2^-$ and h$^+$ are the critical species. $^\bullet$O$_2^-$ could be formed through the direct interaction of photogenerated electrons with the surface adsorbed oxygen of the photocatalyst. This interaction could be depicted as the following Eq. (5):

$$O_2 + e^- \rightarrow {}^\bullet O_2^- \tag{5}$$

3.4.2. Potential degradation mechanisms

It is well known that separation efficiency of electron-hole pairs is a crucial factor for photocatalytic activity of photocatalysts [69,70]. Comparing with the pure $Bi_4Ti_3O_{12}$ and $g-C_3N_4$, the $g-C_3N_4/Bi_4Ti_3O_{12}$ hybrid photocatalyst exhibits much higher photocatalytic activity. It indicates that the composite has a good efficiency in the separation of electron-hole pairs. In order to clarify the enhanced photocatalytic activity mechanism over the composite photocatalyst, the band structure and density of states of $Bi_4Ti_3O_{12}$ and $g-C_3N_4$ were respectively calculated by density functional theory (DFT) in Fig. 9.

$Bi_4Ti_3O_{12}$ is a wide band-gap semiconductor with band-gap energy of 2.832 eV (Fig. 9b), while $g-C_3N_4$ has relatively narrow band-gap energy of 2.69 eV (Fig. 9d). They are closed to the experimental values by DSR spectra. For $Bi_4Ti_3O_{12}$, the conduction band (CB) edge is basically composed of Ti 3d and O 2p orbits, while the valence band (VB) edge is mainly made up of Ti 3d, O 2p and Bi 6p orbits. The O atoms well hybridized with adjacent Ti and Bi atoms in the VB so that the valence-band electrons are difficult to be excited. It is due to the fact that large hybrid electron density of O atoms with adjacent Ti and Bi atoms enhances electrostatic attraction between the nuclear and electrons. However, lower hybrid electron density of Bi atoms with adjacent O and Ti atoms in the CB reduces electrostatic attraction between the nuclear and electrons, making CB electrons easily migrate to the surface of $Bi_4Ti_3O_{12}$. It effectively avoids recombination of electron–hole pairs. In contrast to $Bi_4Ti_3O_{12}$, the CB edge mainly consists of C 2p and N 2p orbits while the VB edge of $g-C_3N_4$ was basically made up of N 2p orbit. The low hybridization of N atoms with adjacent C atoms in the VB implies that the VB electrons are easily to be excited. Nevertheless, owning to the large hybrid electron density of C atoms with adjacent N atoms in the CB, the CB electrons mostly transfer inside the $g-C_3N_4$ to cause high recombination of electron–hole pairs.

Based on the above discussions, $g-C_3N_4$ loaded $Bi_4Ti_3O_{12}$ will decrease the hybrid electron density in the CB of $g-C_3N_4$, which favors CB electrons to transfer to the surface of $Bi_4Ti_3O_{12}$ and hinders recombination of electron-hole pairs. Meanwhile, the existence of $g-C_3N_4$ will also cause the decline of hybrid electron density in the VB of $Bi_4Ti_3O_{12}$, which is beneficial for VB electrons jumping into the CB. Therefore, the combination of $g-C_3N_4$ loaded $Bi_4Ti_3O_{12}$ can achieve efficient separation of electron-hole pairs and thus enhance photocatalytic activity of $g-C_3N_4/Bi_4Ti_3O_{12}$ hybrid photocatalysts.

In photocatalytic systems, the $p–n$ heterojunction structure also plays an important role in accelerating the efficient separation of electron-hole pairs and improving the photocatalytic performance [71,72]. Theoretically, when a number of $p–n$ heterojunction between p-type $g-C_3N_4$ and n-type $Bi_4Ti_3O_{12}$ are formed through ball milling process, electrons from the n-type $Bi_4Ti_3O_{12}$ in the junction interfaces will transfer to the p-type $g-C_3N_4$. Because these holes tend to stay at lower-energy states, it will cause positively charged holes in the n-type $Bi_4Ti_3O_{12}$ and extra negatively charged electrons in the p-type $g-C_3N_4$ [73]. As a consequence, an internal electric field ($E_{internal}$) is simultaneously formed with a negatively charged portion at the interface of the p-type $g-C_3N_4$ region and a positively charged portion at the interface of the n-type $Bi_4Ti_3O_{12}$ region. The direction of an internal electric field is from $Bi_4Ti_3O_{12}$ to $g-C_3N_4$. Thus, the photogenerated electrons and holes are separated efficiently, and the photocatalytic activity is enhanced. Furthermore, the photocatalytic property of the photocatalyst is associated with its band structure. The conduction band (CB) and valence band (VB) potentials of the two semiconductors at the point of zero charge can be calculated by Eqs. (3) and (4) listed as follows [74]:

$$E_{CB} = X - E^e - \frac{1}{2}E_g \tag{3}$$

$$E_{VB} = E_{CB} + E_g \tag{4}$$

Where X is the absolute electronegativity of the semiconductor, E^e is the energy of free electrons on the hydrogen scale (4.5 eV), and Eg is the band gap of the semiconductor. The position of the CB and the VB for $Bi_4Ti_3O_{12}$ and $g-C_3N_4$ crystallites, calculated according to the equation, are shown in Fig. 10a.

$Bi_4Ti_3O_{12}$ and $g-C_3N_4$ adsorb photons of energy, exciting the electrons in the VB to the CB in both $Bi_4Ti_3O_{12}$ and $g-C_3N_4$, leaving holes in the VB. Based on the band energy structure, the electrons in the CB of the p-type $g-C_3N_4$ can easily transfer to the n-type $Bi_4Ti_3O_{12}$. The electrons in the CB of n-type $Bi_4Ti_3O_{12}$ initiate the photocatalytic oxidation. The transformation orientation of holes is opposite, which in the VB of n-type $Bi_4Ti_3O_{12}$ can transfer to the p-type $g-C_3N_4$. Thus, an effective separation of photoexcited electron–hole in $p–n$ junction photocatalyst can be attributed to inner electric field assisted charge transfer at the junction interfaces between the semiconductors with matching band potentials [75].

Moreover, the VB potential of $g-C_3N_4$ (1.56 eV) is not positive enough compared with the standard reduction potential of $\bullet OH/H_2O$ (2.27 eV) or $\bullet OH/OH^-$ (2.38 eV) indicating that the most of h^+ on the surface of $g-C_3N_4$ cannot oxidize H_2O or OH^- into $\bullet OH$. Thus, the photocatalytic degradation of AO-7 can be primarily attributed to the direct reaction with h^+ instead of $\bullet OH$ radicals. In addition, the single electron reduction potential of O_2 is −0.046 eV [76]. Accordingly, the CB potential of $Bi_4Ti_3O_{12}$ (−0.05 eV) is negative to reduce the O_2 to the $\bullet O_2^-$ radicals. The result demonstrates that $\bullet O_2^-$ and h^+ radicals are the main reactive species, coinciding with the results concerning the role of reactive species. Based on the above analysis and discussion, the formation model for the $p–n$ junction photocatalyst and the schematic drawing of electron–hole separation process are illustrated in Fig. 10b.

3.4.3. Identification of intermediate products

GC–MS analysis was used to identify the formation and characterization of intermediates, in order to evaluate the practical applicability of photocatalytic process. The intermediate products formed in the photocatalytic degradation of AO-7 were identified by the analysis of mass spectra obtained from GC–MS applications and were compared with the library data of NIST. Fourteen products were identified based on the mass fragment peaks. The chemical structures of the compound detected by GC/MS along with their retention time and molecular weights are presented in Table 2.

In the primary photocatalytic degradation of AO-7, the attack of reactive species such as h^+, $\bullet O^{2-}$ and $\bullet OH$ make the breaking of the azo bond, the most active group in the structure [77], which produces A and G. The hydroxylation of these intermediates to hydroxylated (G) or polyhydroxylated (H) derivatives are oxidized in turn to the quinoid structures (B, C, I), carboxylic acid structures (D, E, F). Polyhydroxylated, quinoid structures and carboxylic acid structures are unstable and lead to be oxidized through ring–rupturing reactions into short-chain carboxylic acids (J, K). These short-chain carboxylic acid intermediates are presumably further oxidized into aliphatic compounds including L, M and N. Finally, the mineralization reaction to carbon dioxide and water may occur. Thus, in this work, it was proposed that the photocatalytic degradation pathways of AO-7 in water with $N_{10}Bi_{16}$, as illustrated in Fig. 11.

4. Conclusions

The novel $p–n$ heterojunction photocatalyst $g-C_3N_4/Bi_4Ti_3O_{12}$ was successfully fabricated by ball milling process. In comparison to pure $Bi_4Ti_3O_{12}$ and $g-C_3N_4$ samples, the $p–n$ heterojunction photocatalyst $g-C_3N_4/Bi_4Ti_3O_{12}$ exhibits a high photocatalytic behavior for the decomposition of AO-7. The enhanced photocatalytic perfor-

mance could be attributed to the formation of the junction between g-C$_3$N$_4$ and Bi$_4$Ti$_3$O$_{12}$, which suppressed the recombination of photogenerated electron–hole pairs. The amount of g-C$_3$N$_4$ and the time of ball milling were also investigated to optimize the preparation conditions of photocatalysts. The mechanisms of the influence on the photocatalytic performance were finally explained according to the semiconductor energy band theory and the formation of an internal electrostatic field. Moreover, the analysis of reactive species during the photodegradation of AO-7 confirmed that •O$_2^-$ and h$^+$ radicals are the main reactive species. Based on the intermediates identified by GC–MS, the degradation pathways of AO-7 were proposed. It was demonstrated that the breaking of the azo bond by radical oxidation was the major mechanism of AO-7 degradation. The AO-7 molecule was initially decomposed into phenyl and naphthalene intermediates, which were further degraded into ring-opening products and finally mineralized to yield CO$_2$ and H$_2$O.

Acknowledgements

Appendix A. Supplementary data

Supplementary data associated with this article can be found, in the online version, at http://dx.doi.org/10.1016/j.apcatb.2016.03.054.

References

[1] W. Wu, S. Zhang, F. Ren, X. Xiao, J. Zhou, C. Jiang, Nanoscale 3 (2011) 4676–4684.
[2] X. Wang, K. Maeda, A. Thomas, K. Takanabe, G. Xin, J.M. Carlsson, K. Domen, M. Antonietti, Nat. mater. 8 (2009) 76–80.
[3] X.Q. Qiu, L.P. Li, J. Zheng, J.J. Liu, X.F. Sun, G.S. Li, J. Phys. Chem. C 112 (2008) 12242–12248.
[4] S.C. Yan, S.B. Lv, Z.S. Li, Z.G. Zou, Dalton Trans. 39 (2010) 1488–1491.
[5] H.X. Li, Z.F. Bian, J. Zhu, D.Q. Zhang, G.S. Li, Y.N. Huo, H. Li, Y.F. Lu, J. Am. Chem. Soc. 129 (2007) 8406–8407.
[6] A. Fujishima, K. Honda, Nature 238 (1972) 37–38.
[7] H. Tong, S. Ouyang, Y. Bi, N. Umezawa, M. Oshikiri, J. Ye, Adv. mater. 24 (2012) 229–251.
[8] S.G. Kumar, L.G. Devi, J. Phys. Chem. A 115 (2011) 13211–13241.
[9] H.B. Fu, C.S. Pan, W.Q. Yao, Y.F. Zhu, J. Phys. Chem. B 109 (2005) 22432–22439.
[10] Z. Zhang, W. Wang, L. Wang, S. Sun, ACS Appl. Mater. Interfaces 4 (2012) 593–597.
[11] T. Kamegawa, S. Matsuura, H. Seto, H. Yamashita, Angew. Chem. Int. Ed. 52 (2013) 916–919.
[12] W.F. Yao, X.H. Xu, H. Wang, J.T. Zhou, X.N. Yang, Y. Zhang, S.X. Shang, B.B. Huang, Appl. Catal. B-Environ. 52 (2004) 109–116.
[13] C. Pan, Y. Zhu, Environ. Sci. Technol. 44 (2010) 5570–5574.
[14] D. Hou, W. Luo, Y. Huang, J.C. Yu, X. Hu, Nanoscale 5 (2013) 2028–2035.
[15] W.F. Yao, H. Wang, X.H. Xu, S.X. Shang, Y. Hou, Y. Zhang, M. Wang, Mater. Lett. 57 (2003) 1899–1902.
[16] Y. Wang, X. Wang, M. Antonietti, Angew. Chem. 51 (2012) 68–89.
[17] S.C. Yan, Z.S. Li, Z.G. Zou, Langmuir 25 (2009) 10397–10401.
[18] M. Groenewolt, M. Antonietti, Adv. Mater. 17 (2005) 1789–1792.
[19] Q. Xiang, J. Yu, M. Jaroniec, J. Phys. Chem. C 115 (2011) 7355–7363.
[20] S.C. Yan, Z.S. Li, Z.G. Zou, Langmuir 26 (2010) 3894–3901.
[21] X. Bai, R. Zong, C. Li, D. Liu, Y. Liu, Y. Zhu, Appl. Catal. B-Environ. 147 (2014) 82–91.
[22] N. Liang, J. Zai, M. Xu, Q. Zhu, X. Wei, X. Qian, J. Mater. Chem. A 2 (2014) 4208–4216.
[23] L. Yang, S. Luo, Y. Li, Y. Xiao, Q. Kang, Q. Cai, Environ. Sci. Technol. 44 (2010) 7641–7646.
[24] J. Zhang, M. Zhang, R.-Q. Sun, X. Wang, Angew. Chem. Int. Ed. 51 (2012) 10145–10149.
[25] H. Li, J. Liu, W. Hou, N. Du, R. Zhang, X. Tao, Appl. Catal. B-Environ. 160 (2014) 89–97.
[26] T. Cao, Y. Li, C. Wang, Z. Zhang, M. Zhang, C. Shao, Y. Liu, J. Mater. Chem. 21 (2011) 6922–6927.
[27] L. Sun, Y. Qi, C.-J. Jia, Z. Jin, W. Fan, Nanoscale 6 (2014) 2649–2659.
[28] K. Li, S. Gao, Q. Wang, H. Xu, Z. Wang, B. Huang, Y. Dai, J. Lu, ACS Appl. Mater. Interfaces 7 (2014) 9023–9030.
[29] F.-t. Li, Q. Wang, J. Ran, Y.-j. Hao, X.-j. Wang, D. Zhao, S.Z. Qiao, Nanoscale 7 (2015) 1116–1126.
[30] H. Wang, L. Zhang, Z. Chen, J. Hu, S. Li, Z. Wang, J. Liu, X. Wang, Chem. Soc. Rev. 43 (2014) 5234–5244.
[31] M. Ge, C. Cao, S. Li, S. Zhang, S. Deng, J. Huang, Q. Li, K. Zhang, S.S. Al-Deyab, Y. Lai, Nanoscale 7 (2015) 11552–11560.
[32] Z.Q. He, Y.Q. Shi, C. Gao, L.N. Wen, J.M. Chen, S. Song, J. Phys. Chem. C 118 (2014) 389–398.
[33] D. Hou, X. Hu, P. Hu, W. Zhang, M. Zhang, Y. Huang, Nanoscale 5 (2013) 9764–9772.
[34] N. Liang, M. Wang, L. Jin, S.S. Huang, W.L. Chen, M. Xu, Q.Q. He, J.T. Zai, N.H. Fang, X.F. Qian, ACS Appl. Mater. Interfaces 6 (2014) 11698–11705.
[35] A.E. Kandjani, Y.M. Sabri, S.R. Periasamy, N. Zohora, M.H. Amin, A. Nafady, S.K. Bhargava, Langmuir 31 (2015) 10922–10930.
[36] M. Han, T. Sun, P.Y. Tan, X. Chen, O.K. Tan, M.S. Tse, RSC Adv. 3 (2013) 24964.
[37] J.G. Hou, C. Yang, H.J. Cheng, S.Q. Jiao, O. Takeda, H.M. Zhu, Energy Environ. Sci. 7 (2014) 3758–3768.
[38] W. Zhao, Y. Jin, C.H. Gao, W. Gu, Z.M. Jin, Y.L. Lei, L.S. Liao, Mater. Chem. Phys. 143 (2014) 952–962.
[39] S.L. James, C.J. Adams, C. Bolm, D. Braga, P. Collier, T. Friscic, F. Grepioni, K.D.M. Harris, G. Hyett, W. Jones, A. Krebs, J. Mack, L. Maini, A.G. Orpen, I.P. Parkin, W.C. Shearouse, J.W. Steed, D.C. Waddell, Chem. Soc. Rev. 41 (2012) 413–447.
[40] K. Ralphs, C. Hardacre, S.L. James, Chem. Soc. Rev. 42 (2013) 7701–7718.
[41] S. Chen, S. Zhang, W. Zhao, W. Liu, J. Nanopart. Res. 11 (2009) 931–938.
[42] H.X. Zhao, H.T. Yu, X. Quan, S. Chen, Y.B. Zhang, H.M. Zhao, H. Wang, Appl. Catal. B-Environ. 152 (2014) 46–50.
[43] H.S. Gu, P.Z. Chen, Y.H. Zhou, M. Zhao, A.X. Kuang, X.J. Li, Ferroelectrics 211 (1998) 271–280.
[44] Y.M. Kan, X.H. Jin, G.J. Zhang, P.L. Wang, Y.B. Cheng, D.S. Yan, J. Mater. Chem. 14 (2004) 3566–3570.
[45] Y. Wang, R. Shi, J. Lin, Y. Zhu, Energy. Environ. Sci. 4 (2011) 2922–2929.
[46] J. Fu, B. Chang, Y. Tian, F. Xi, X. Dong, J. Mater. Chem. A 1 (2013) 3083–3090.
[47] S. Wang, D. Li, C. Sun, S. Yang, Y. Guan, H. He, Appl. Catal. B-Environ. 144 (2014) 885–892.
[48] S. Martha, A. Nashim, K.M. Parida, J. Mater. Chem. A 1 (2013) 7816–7824.
[49] Y. Li, H. Zhang, P. Liu, D. Wang, Y. Li, H. Zhao, Small 9 (2013) 3336–3344.
[50] Z. Chen, H. Jiang, W. Jin, C. Shi, Appl. Catal. B-Environ. 180 (2016) 698–706.
[51] C. Li, S. Wang, T. Wang, Y. Wei, P. Zhang, J. Gong, Small 10 (2014) 2783–2790 (2741).
[52] N. Tian, H. Huang, C. Liu, F. Dong, T. Zhang, X. Du, S. Yu, Y. Zhang, J. Mater. Chem. A 3 (2015) 17120–17129.
[53] L. Ge, C. Han, J. Liu, Appl. Catal. B-Environ. 108 (2011) 100–107.
[54] J.W. Tang, Z.G. Zou, J.H. Ye, J. Phys. Chem. B 107 (2003) 14265–14269.
[55] S. Kumar, T. Surendar, A. Baruah, V. Shanker, J. Mater. Chem. A 1 (2013) 5333–5340.
[56] F. Dong, Z. Zhao, T. Xiong, Z. Ni, W. Zhang, Y. Sun, W.-K. Ho, ACS Appl. Mater. Interfaces 5 (2013) 11392–11401.
[57] D.C. Lee, I. Robel, J.M. Pietryga, V.I. Klimov, J. Am. Chem. Soc. 132 (2010) 9960–9962.
[58] K. Lv, X. Li, K. Deng, J. Sun, X. Li, M. Li, Appl. Catal. B-Environ. 95 (2010) 383–392.
[59] J. Yu, G. Wang, B. Cheng, M. Zhou, Appl. Catal. B-Environ. 69 (2007) 171–180.
[60] Y.J. Li, X.D. Li, J.W. Li, J. Yin, Water Res. 40 (2006) 1119–1126.
[61] K. Li, S. Gao, Q. Wang, H. Xu, Z. Wang, B. Huang, Y. Dai, J. Lu, ACS Appl. Mater. Interfaces 7 (2015) 9023–9030.
[62] S. Chen, W. Zhao, W. Liu, S. Zhang, Appl. Surf. Sci. 255 (2008) 2478–2484.
[63] J.S. Wang, S. Yin, M. Komatsu, Q.W. Zhang, F. Saito, T. Sato, J. Photochem. Photobiol. A-Chem. 165 (2004) 149–156.
[64] B. Subash, B. Krishnakumar, M. Swaminathan, M. Shanthi, Langmuir 29 (2013) 939–949.
[65] R. Jiang, H. Zhu, X. Li, L. Xiao, Chem. Eng. J. 152 (2009) 537–542.
[66] X.F. Zhou, C. Hu, X.X. Hu, T.W. Peng, J.H. Qu, J. Phys. Chem. C 114 (2010) 2746–2750.
[67] W. Zhao, Y. Guo, Y. Faiz, W.-T. Yuan, C. Sun, S.-M. Wang, Y.-H. Deng, Y. Zhuang, Y. Li, X.-M. Wang, H. He, S.-G. Yang, Appl. Catal. B-Environ. 163 (2015) 288–297.
[68] L.-S. Zhang, K.-H. Wong, H.-Y. Yip, C. Hu, J.C. Yu, C.-Y. Chan, P.-K. Wong, Environ. Sci. Technol. 44 (2010) 1392–1398.
[69] Y. Wang, X. Bai, C. Pan, J. He, Y. Zhu, J. Mater. Chem. 22 (2012) 11568–11573.
[70] J. Fu, Y. Tian, B. Chang, F. Xi, X. Dong, J. Mater. Chem. 22 (2012) 21159–21166.
[71] J. Zhang, S.Z. Qiao, L.F. Qi, J.G. Yu, Phys. Chem. Chem. Phys. 15 (2013) 12088–12094.
[72] Z. Zhang, C. Shao, X. Li, C. Wang, M. Zhang, Y. Liu, ACS Appl. Mater. Interfaces 2 (2010) 2915–2923.
[73] W. Wang, X. Huang, S. Wu, Y. Zhou, L. Wang, H. Shi, Y. Liang, B. Zou, Appl. Catal. B-Environ. 134 (2013) 293–301.
[74] X. Li, J. Zhu, H. Li, Appl. Catal. B-Environ. 123 (2012) 174–181.
[75] X. Zhang, L. Zhang, T. Xie, D. Wang, J. Phys. Chem. C 113 (2009) 7371–7378.
[76] D. Wang, T. Kako, J. Ye, J. Am. Chem. Soc. 130 (2008) 2724–2725.
[77] I.K. Konstantinou, T.A. Albanis, Appl. Catal. B-Environ. 49 (2004) 1–14.